The effect of nano-sized κ-carbides on the mechanical properties of an Fe-Mn-Al-C alloy

Banis, Alexandros; Gomez, Andrea; Dutta, Aniruddha; Sabirov, Ilchat; Petrov, Roumen H.

DOI
10.1016/j.matchar.2023.113364

Publication date
2023

Document Version
Final published version

Published in
Materials Characterization

Citation (APA)
Banis, A., Gomez, A., Dutta, A., Sabirov, I., & Petrov, R. H. (2023). The effect of nano-sized κ-carbides on the mechanical properties of an Fe-Mn-Al-C alloy. *Materials Characterization*, *205*, Article 113364. https://doi.org/10.1016/j.matchar.2023.113364

Materials Characterization 205 (2023) 113364

Contents lists available at ScienceDirect

Materials Characterization

journal homepage: www.elsevier.com/locate/matchar

The effect of nano-sized κ-carbides on the mechanical properties of an Fe-Mn-Al-C alloy

Alexandros Banis [a,*], Andrea Gomez [b], Aniruddha Dutta [c], Ilchat Sabirov [b], Roumen H. Petrov [a,d]

[a] Department of Electromechanical, Systems and Metal Engineering, Ghent University, Ghent, Belgium
[b] IMDEA Materials Institute, Getafe, Madrid, Spain
[c] ArcelorMittal Global R&D, Ghent, Belgium
[d] Department of Materials Science and Engineering, Delft University of Technology, Delft, the Netherlands

ARTICLE INFO

Keywords:
Low-density steels
κ-Carbides
Aging
Microstructure characterization
micro-band induced plasticity

ABSTRACT

The strengthening via precipitation of nano-sized κ-carbides leads to exceptional strength-ductility balance in low-density steels. During aging, such nanocarbides form through spinodal decomposition by fluctuations in the aluminum and carbon content in the austenite, followed by short-range ordering. At lower aging temperatures and short aging times, the κ-carbides are very fine, coherent with the matrix, and homogeneously distributed. When the aging temperature increases, heterogeneous nucleation initiates on the grain boundaries, and the κ-carbides become coarse and lose coherency with the austenite matrix, leading to the deterioration of the mechanical properties. This work studies a fully austenitic hot rolled Fe-29Mn-8.7Al-0.9C alloy after different aging treatments. Two aging treatments were selected for a detailed study of the microstructure based on the exceptional strength-ductility balance demonstrated by these conditions. The samples aged at 550 °C for 8 h exhibited an ultimate tensile strength of 1141 MPa and strain at failure around 49%. The second aging treatment selected was aging at 600 °C for 1 h, and these samples exhibited an ultimate tensile strength of 1084 MPa, with strain at failure 62%. The size and morphology of the austenite grains and the annealing twins were studied through EBSD. Additionally, the size, morphology, and volume fraction of the nano-sized κ-carbides were studied using TEM. Both aging conditions led to microstructures consisting of a matrix formed by equiaxed austenite grains with homogeneously distributed intragranular κ-carbides. The κ-carbides were coherent with the matrix and showed globular morphology with a diameter between 3 and 6 nm and coherent with the austenite matrix. The interaction between gliding dislocations and κ-carbides was analyzed. It was shown that the mechanical behavior of the studied material is characterized by very high sensitivity to the size of κ-carbides and, therefore, can be tailored by appropriate aging treatment.

1. Introduction

Low-density steels have been the subject of many studies in the past years. Their exceptional strength-ductility balance attracts the interest of many research groups as they pose an alternative option for applications in the automotive industry. Chen [1] and Zambrano [2] have conducted extensive overviews on the current state of the art of such alloys. The high aluminum (Al) content decreases the steel's density by expanding the lattice parameter and thus results in weight reduction [3,4]. On the other hand, the high manganese (Mn) content leads to fully austenitic microstructures at room temperature [5]. According to the literature [6,7], alloying the steel with 5–11 wt% Al and 0.3–1.2 wt% carbon (C) makes it age-hardenable through the precipitation of κ-carbides. Such carbides are an ordered metastable phase with an $L1_2$ perovskite-type structure [8], composition $(Fe,Mn)_3AlC_x$ ($x < 1$), and with a cube-on-cube orientation with the austenite matrix [9,10]. They form in the temperature range between 450 and 650 °C through chemical modulation of Al, C followed by Short-Range Ordering (SRO). The formation of the κ-carbides leads to precipitation hardening of the steel caused by interaction between the κ-carbides and the mobile dislocations during plastic deformation [11]. Though, at higher aging temperatures (650–800 °C), intergranular formation of κ-carbides initiates on the γ/γ grain boundaries. These carbides have faster growth kinetics than the intragranular carbides due to higher local energy at

* Corresponding author.
E-mail address: Alexandros.banis@ugent.be (A. Banis).

https://doi.org/10.1016/j.matchar.2023.113364
Received 7 June 2023; Received in revised form 4 September 2023; Accepted 28 September 2023
Available online 29 September 2023

grain boundaries [12–15]. Previous work from the authors [16] has shown that the intragranular κ-carbides favor the properties of the Fe-Mn-Al-C alloys, as they increase their strength without compromising their ductility due to their ordered structure and coherency with the matrix. On the other hand, intergranular κ-carbides should be avoided, as they can dramatically degrade their mechanical performance [17].

These types of steel have a high Stacking Fault Energy (SFE) due to the high Al content, and thus the deformation mechanism changes from Twinning Induced Plasticity (TWIP) to dislocation slip [18]. Yoo et al. [19] described the glide planar softening effect in which the leading dislocation moving through the lattice will eventually face the energy barrier by SRO. Then, assisted by the piling of the following dislocations activated on the same single slip plane, it will overcome the SRO energy barrier by destroying it. On the next stage, the following dislocations will glide more easily over the destroyed SRO region on that plane following the leading dislocation. According to Frommeyer et al. [4], the excellent combination of strength and ductility of these steels is attributed to the micro-band induced plasticity (MBIP).

This article focuses on the microstructure and related mechanical behavior of a fully austenitic hot rolled Fe-29Mn-8.7Al-0.9C steel after two different aging treatments at temperatures below 650 °C, which promotes the formation of intragranular κ-carbides while suppressing the formation of intergranular κ-carbides. The aging parameters determine the morphology, size, and volume fraction of intragranular κ-carbides, which in turn should affect their deformation behavior [11,16]. The aim of this research is to explore the sensitivity of tensile mechanical behavior (strength and ductility) to the size of intragranular nano-sized k-carbides as well as the effect of the latter on the dislocation – κ-carbide interaction during plastic deformation.

2. Materials and methodology

An Fe-29Mn-8.7Al-0.9C (wt%) steel was selected for this study. The casted ingots were reheated to a temperature of 1200 °C and hot-rolled to a final thickness of 5 mm, with a total reduction ratio of 65%. After the last rolling pass, the sheets were directly quenched in water to avoid the formation of intergranular κ-carbides. Samples were cut off from the sheets and were aged in the muffle furnace, inside a sand bath under strict control of the temperature and time. The selected aging conditions and sample names are given below in Table 1:

The aging temperature and time were selected after literature review and after hardness measurements. From these experiments, it was shown that the peak aging conditions i.e., maximum hardness was achieved after 8 h of aging at 550 °C, and 1 h of aging at 600 °C. After the aging, the pieces were cooled in the air, and smaller samples were cut so that the rolling's Transverse Direction (TD) could be observed in the microscope.

For the Electron Back-Scatter Diffraction (EBSD) analysis, the standard metallographic preparation consisting of grinding (up to #2000 SiC paper) followed by polishing (diamond pastes of 3 μm, 1 μm, and 0.1 μm colloidal silica) was performed. An FEI Quanta TM 450-FEG-SEM was used for the EBSD analysis using the following settings: 20 kV voltage, with an aperture size of 50 μm, a probe current of 2.4 nA, a working distance of 15 μm, and back-scatter electron (BSE) imaging. For EBSD analysis, the sample was tilted 70° towards the vertical axis. The corresponding orientation data were post-processed with EDAX-TSL-OIM-Data Analysis version 7.3.1. software using the following grain definition: misorientation with neighboring grains higher than 15°, a minimum number of points per grain was 8, and a confidence index (CI) larger than 0.1. Additional maps were obtained to analyze the austenite grain morphology and the annealing twins, with a scan size of 100 × 100 μm and a step size of 100 nm. The grain definition for these maps is the same as the one mentioned above.

Table 1
The names and aging conditions of the studied samples.

Sample name	HR&WQ	550_8	600_1
Aging temperature (°C)	–	550	600
Aging time (h)	–	8	1

For Transmission Electron Microscopy (TEM) analysis, samples were produced by grinding up to a thickness of 100 μm and using electrolytic preparation equipment with perchloric acid. A Jeol JEM-2200FS, 200 kV field emission TEM was used.

For the Transmission Kikuchi Diffraction (TKD) analysis, the same TEM samples were placed on the specific holder with a tilt towards the EBSD detector of −30°. The working distance was 5 mm, and the step size used 6 nm. The voltage was set to 20 kV, with a final aperture size of 50 μm and a probe current of ~2.4 nA.

Finally, for the tensile tests, sub-size samples with a gauge length of 25 mm according to the ASTM E8 standard geometry were cut from the hot-rolled sheets parallel to the rolling direction. The strain rate for the tensile tests was 10^{-3} s^{-1}, and 3 samples per condition were tested. The results were found to be reproducible.

3. Results

3.1. Austenite morphology

The microstructure of the hot-rolled and water-quenched (HR&WQ) sample consists of austenite grains with annealing twins. The Normal Direction (ND) Inverse Pole Figure (IPF) maps (Fig. 1a-c) show the orientations of the grains and the twins with different colors, and it can be seen that no orientation is preferred. The presence of annealing twins adds more orientations to the microstructure. These twins are distinguished by the Σ3 twin boundaries ⟨111⟩60° shown as yellow in the Grain Average Image Quality (GAIQ) maps of Fig. 1d-f. The total number of grains in the scan minus the grains excluding twins determines the average number of annealing twins within a parent austenite grain. Then, dividing the number of twins by the total number of grains gives the ratio of twins per grain. This methodology for calculating the twin density was used by Field et al. [20] to determine the twin density in recrystallized copper alloys. In Figs. 1 and 2a, the average number of twins per grain is given, as was calculated by the EBSD scans. For example, the total number of grains for the EBSD scan of the HR&WQ sample is 504. Then, the number of grains excluding the annealing twins is 84. Then, the number of annealing twins is 420, and dividing this value by the total number of grains gives an average of 0.833 twins per grain. Similarly, the average number of annealing twins per grain is 0.856 for the 550_8 sample and 0.719 for the 600_1 sample. The grain definitions used for these calculations are a 15° minimum misorientation angle and a minimum grain size of 15 measurement points. The twin boundaries excluded for these calculations are Σ3 type boundaries with a tolerance of 5°. The austenite grains are equiaxed in all samples. The grain morphology and presence of annealing twins in all studied samples indicates that the recrystallization process occurs during the hot rolling, between the passes, and before the final water quenching. Finally, it is observed that these values are almost the same for all of the studied samples, with insignificant deviation, indicating that no recrystallization occurs during the aging process.

The distribution of the austenite grain size with the annealing twins for the studied samples is shown in the diagram of Fig. 2b. The scan size for the austenite grain size analysis was 1000 × 1000 μm, and the step size was 0.6 μm, resulting in maps containing approximately 35,000 grains. All samples have similar grain sizes, on average ~ 8 μm. The peaks of the aged samples are shifted slightly to the right of the diagram, but no significant grain growth is expected to occur at these relatively low aging temperatures.

3.2. Mechanical properties

Tensile tests were performed in the aged samples at a strain rate of

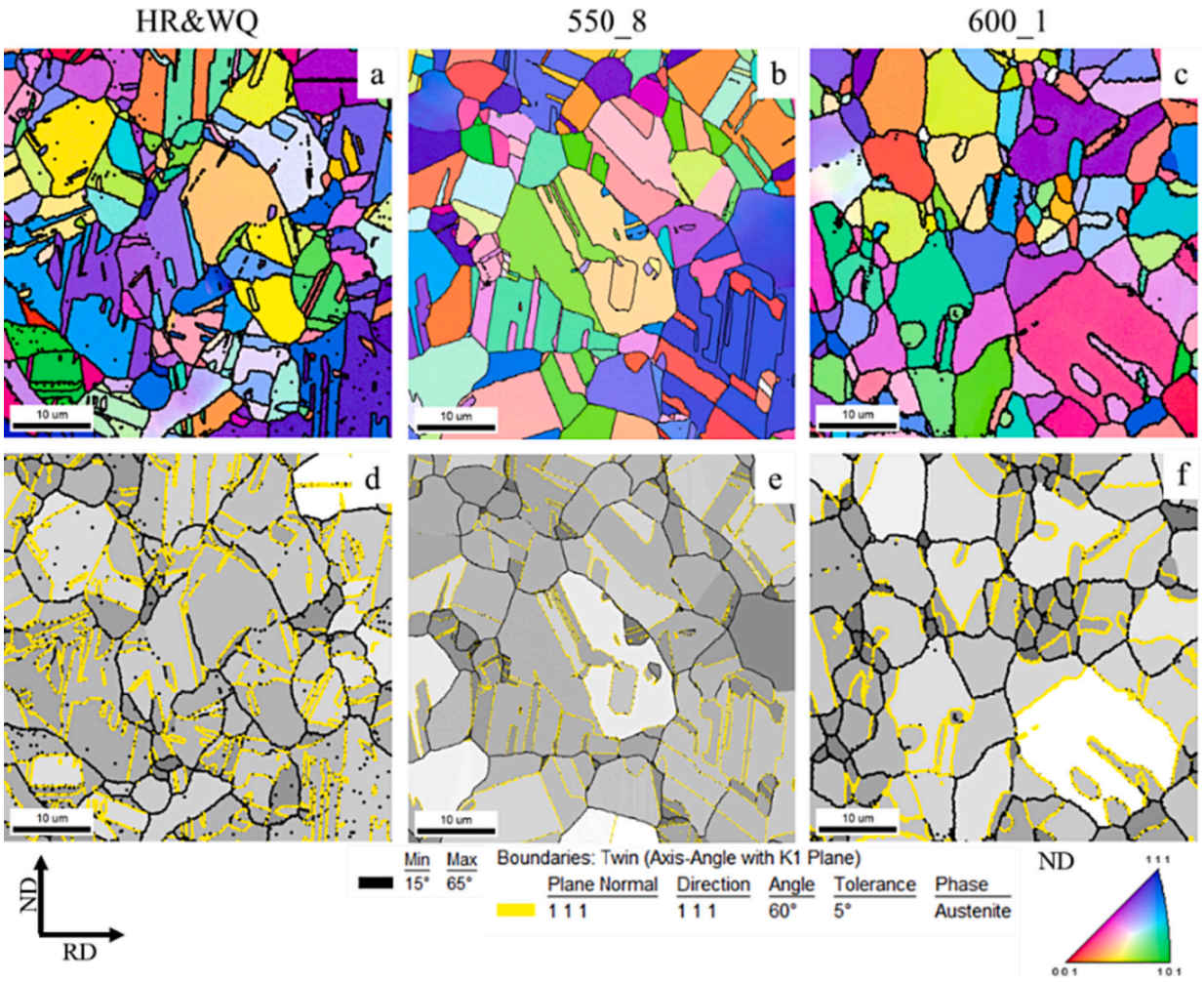

Fig. 1. ND IPF maps of the a) HR&WQ, b) 550_8, and c) 600_1 sample. GAIQ maps with Σ3 twin boundaries plotted in yellow for the d) HR&WQ, e) 550_8, and f) 600_1 sample. (For interpretation of the references to colour in this figure legend, the reader is referred to the web version of this article.)

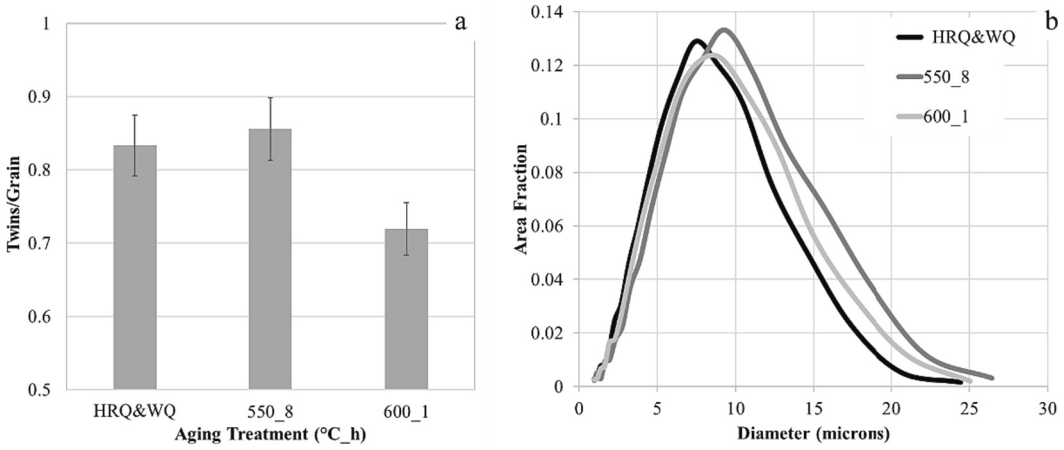

Fig. 2. a) The twin density calculated for the studied samples b) the studied samples' austenite grain size (equivalent circular diameter) distribution.

10^{-3} s^{-1}. In Fig. 3a, the engineering stress-strain curves are shown. Three specimens were tested per condition, but only two representative curves are given in the diagram. In addition, the average values of the tensile properties from all three measurements are given in the imposed table. Both samples exhibited continuous yielding. The 550_8 sample demonstrates higher yield strength (σ_{YS}) of 1015 MPa, compared to the 920.5 MPa exhibited by the 600_1 sample. Then, the Ultimate Tensile Strength (σ_{UTS}) is 1141 and 1084 MPa for the 550_8 and 600_1 samples, respectively. The total strain at failure (ε_{TE}) may reach 49.1% for the 550_8 sample and 61.92% for the 600_1 sample. In Fig. 3b, the true stress and work hardening rates ($d\sigma/d\varepsilon$) are shown as a function of the true strain. For clarity, the polynomial trendline is given as dashed lines for the work hardening rates. It can be observed that for both samples, the work hardening rates show the same trend. At the initial stages of

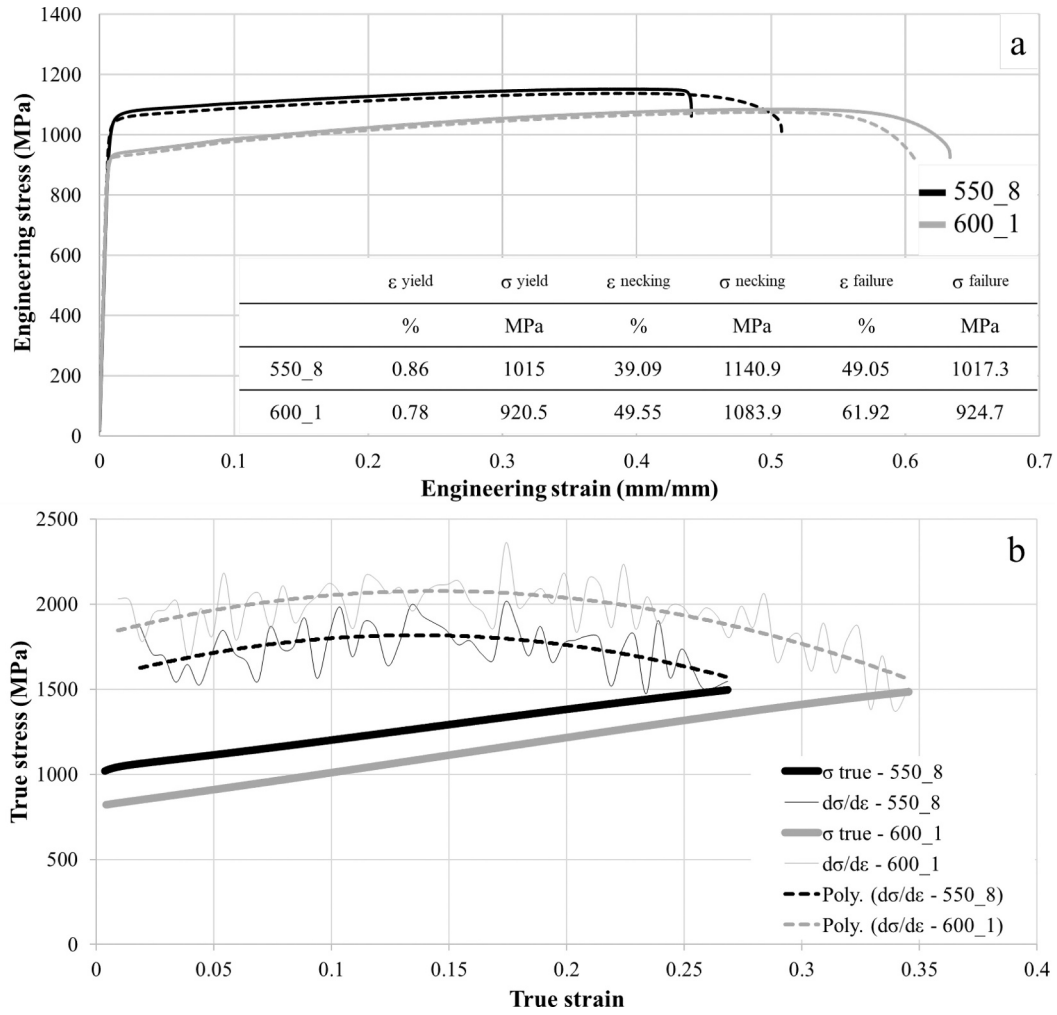

	ε yield	σ yield	ε necking	σ necking	ε failure	σ failure
	%	MPa	%	MPa	%	MPa
550_8	0.86	1015	39.09	1140.9	49.05	1017.3
600_1	0.78	920.5	49.55	1083.9	61.92	924.7

Fig. 3. a) Engineering stress-strain curves for the aged samples. The average values are given in the superimposed table; b) true stress – true strain curves for the aged samples along with the corresponding work hardening rate curves.

strain, the work hardening rate is increasing until it reaches a maximum value, which is 1800 MPa at strain around 0.15 for the 550_8 sample, and 2000 MPa at approximately the same levels of strain for the 600_1. After the maximum value is reached, the work hardening rate decreases for both samples, as the strain increases.

Fractographic analysis performed on the fracture surface of both samples (Fig. 4) shows ductile fracture. The dimple size varies in a wide range from 1 μm to 12 μm, and the aging treatment does not affect the

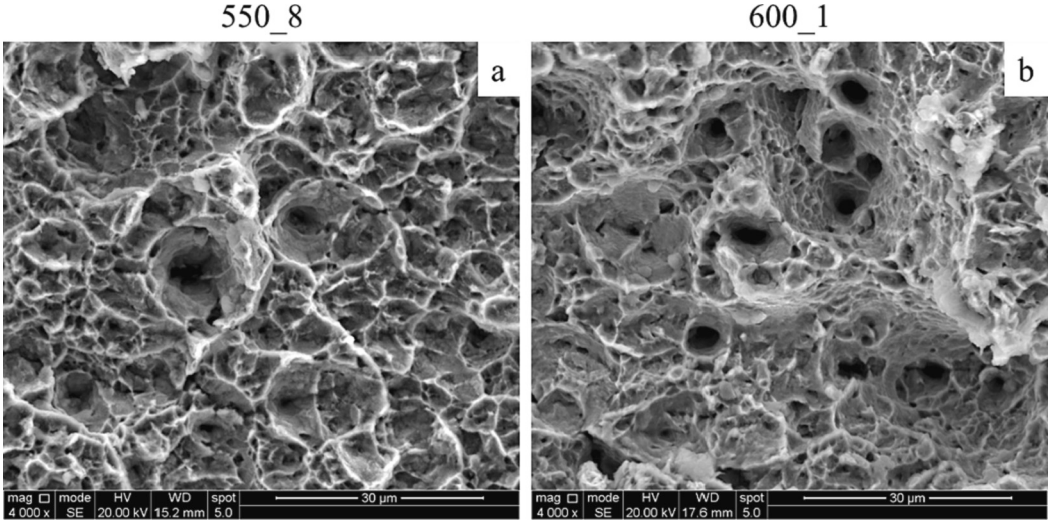

Fig. 4. SEM fractography images of the aged samples after the tensile tests show ductile type of fracture with dimples.

morphology of fracture surface.

4. Discussion

TEM analysis is used to explain the difference in the tensile properties between the aged samples. As aging treatment does not affect the morphology and size of the austenite grains, the precipitation-hardening effect of the κ-carbides seems to be the main reason for the changes in the mechanical properties and it was investigated in detail. Fig. 5 shows the Scanning TEM (STEM) images for the HR&WQ, 550_8, and 600_1 samples. Before the aging stage, no intergranular or intragranular κ-carbides are observed due to the water quenching of the sheets after the final rolling pass. In the aged samples, some very fine particles can be observed inside the grains. Also, it is unclear if precipitation has started on the grain boundaries, but no coarse carbides have been observed.

To better observe the nano-sized κ-carbides, higher magnification was used. Fig. 6a,b show High Resolution (HR) TEM images. The zone axis is [001], and the atoms of the austenite matrix and the κ-carbides can be observed. Using the Inverse Fast Fourier Transformation (IFFT), it is possible to distinguish the κ-carbides, as shown in Fig. 6c,d. In these figures, the atoms belonging to the κ-carbides are shown in white and blue, depending on the intensity of the reflection. At this stage of aging, the κ-carbides have a globular shape and are randomly and homogeneously distributed in the matrix. Their precipitation occurs during the concurrent fluctuations in the chemical composition and SRO [21]. Increasing the aging temperature increases the kinetics of particle coarsening [22], and the κ-carbides obtain cuboidal or plate-like shapes and form parallel stacks with narrow and broad γ-channels in between [23,24]. However, in this case, the increase of the aging temperature from 550 to 600 °C is compensated by the low aging time, and thus, the formation of stacks is avoided.

The observed gradient in the reflection intensity is attributed to the SRO, as no clear phase boundaries can be determined. In addition, the arrangement of the atoms has the same orientation for all of the κ-carbides. This orientation is the same as the austenite matrix, indicating the coherency between the matrix and the carbides.

The size (diameter) of the κ-carbides has been measured for the two samples to quantitatively analyze their effect on tensile properties. The size of the κ-carbides is analyzed in Table 2. The average size of the κ-carbides after aging for 8 h at 550 °C is 2.98 nm, almost double the size of the carbides of the 600_1 sample, which is 1.46 nm. The gaussian distribution of the measurements is also plotted in Fig. 7. It can easily be observed that the curve for the 600_1 sample is shifted to lower diameters, indicating a smaller carbide size. Also, it can be observed that the distribution of carbide size is more narrow for the 600_1 sample, between 0.8 and 2.5 nm, while for the 550_8 sample the distribution of carbide size is wider, between 1.5 and 4.5 nm. This also corresponds to the smaller standard deviation seen in Table 2. This means that for the 550_8 sample, there is larger variation in the size of the κ-carbides.

Based on XRD analysis in Fig. 8, it was observed that the aged samples had peaks that shifted slightly towards the right when compared to the hot-rolled sample. According to Kim [25], compressive strains are imposed on the austenite matrix, whereas tensile strains exerted on the κ-carbides. This explains the shift in peaks and also the slightly broader peak of the 550_8 sample, which had larger κ-carbides that created more strains. In specific, the Full-Width at Half Maximum (FWHM) is measured at 0.267 and 0.258 for the 550_8 and 600_1 samples, respectively. However, the fact that the peaks were in the same position for the aged samples suggests that the lattice parameter of the κ-carbides is similar to that of the austenite matrix and that the fraction of κ-carbides in both samples is almost identical.

This difference in the size of the κ-carbides is attributed to the different aging treatments. It can be assumed that during aging at 600 °C for 1 h, the formation of κ-carbides is less pronounced than in the 550_8 sample, while the volume fraction is similar for both samples. This means that the interparticle spacing or the size of the austenite channels between the carbides is larger in the 600_1 sample. The dislocations glide [26] during deformation and interact with the κ-carbides by shearing them [23,27]. The shearing occurs as the carbides are coherent with the austenite matrix. According to the literature [25,28], the fully coherent κ-carbides reduce the lattice misfit strain, and their precipitation generates a negligible amount of lattice strains, namely $<3\%$. Also, bypassing such small carbides is impossible due to the very small interparticle spacing [29], as in this case. In [23], it was shown for the Fe-30.4Mn-8Al-1.2C aged alloy that the Orowan mechanism is possible if the interparticle spacing is larger than $\sim$20 nm. Therefore, Orowan bypassing of κ-carbide stacks would be possible at later stages of aging and κ-carbide growth [23]. In Fig. 9, the IFFT image of a single κ-carbide is shown. In this IFFT, the atoms that give super-lattice reflections are isolated, namely the ordered atoms. As it appears, the SRO is not clearly visible in the part of the carbide annotated with the yellow dashed line, which is caused by the glide planar softening effect that has been described in [19,27]. Also, a small step can be observed, which indicates that the specific carbide has been sheared by dislocations.

In Fig. 10, the same area of a single grain of the 550_8 sample after tensile deformation with a strain of 2% was studied via STEM (Fig. 10a), DF TEM (Fig. 10b), and TKD (Fig. 10c-e). From the STEM image, the formation of micro-bands can be observed between the dislocation walls [27]. Inside the bands, gliding dislocations also appear. The mobility of these dislocations will depend on their interactions with the nano-sized κ-carbides. As was shown from Fig. 9, the dislocations are shearing the κ-carbides, and therefore their movement will be impeded. Therefore,

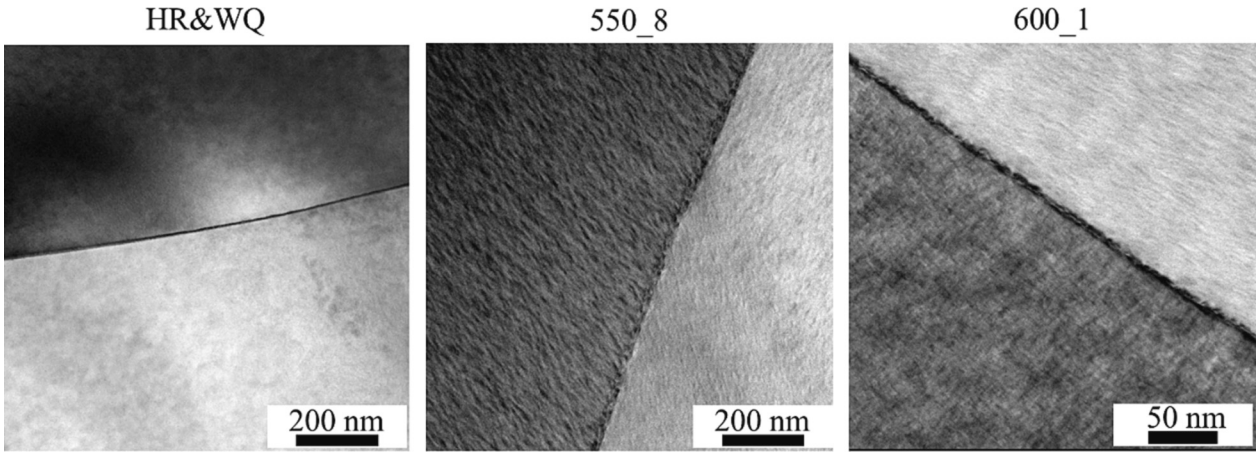

Fig. 5. STEM images of the studied samples showing two austenite grains and a grain boundary. The formation of intergranular κ-carbides is avoided in all conditions.

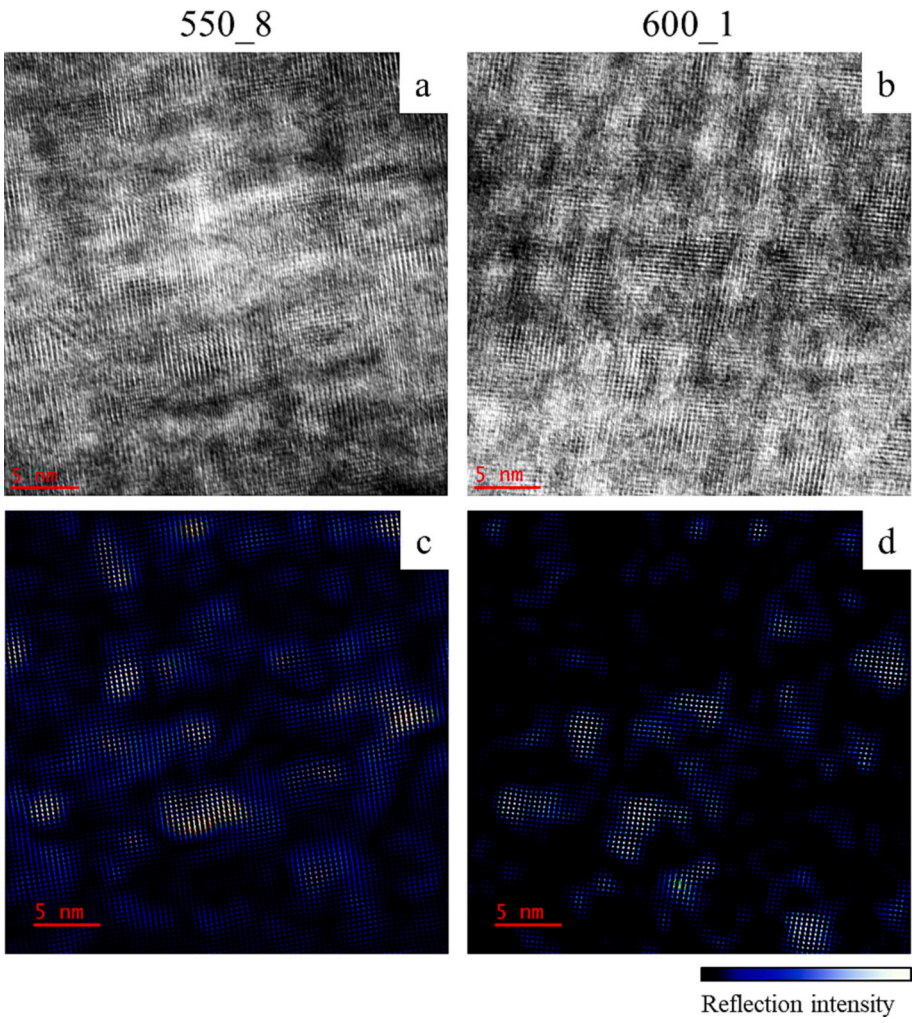

Fig. 6. a,b) HRTEM images of the aged samples on the [001] zone axis. c,d) corresponding IFFT after masking the reflections of the austenite matrix, thus showing the atoms that belong to the κ-carbides.

Table 2
The average diameter of the κ-carbides with the standard deviation (SD) and relative accuracy (RA) of the measurements.

Sample	Diameter (nm)	SD (%)	RA%
550_8	2.98	0.9	9.6
600_1	1.46	0.59	10.4

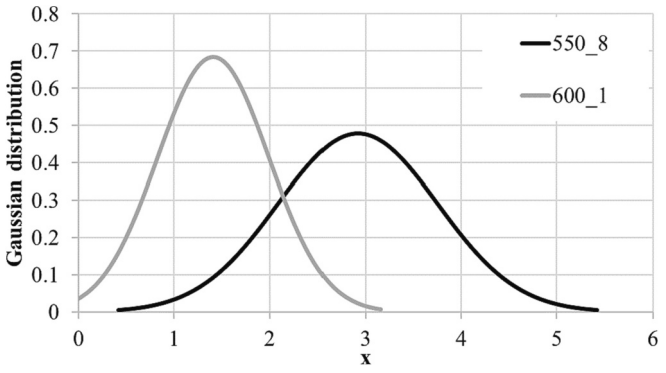

Fig. 7. The gaussian distribution plotted based on the diameter of the κ-carbides for the 550_8 and 600_1 samples.

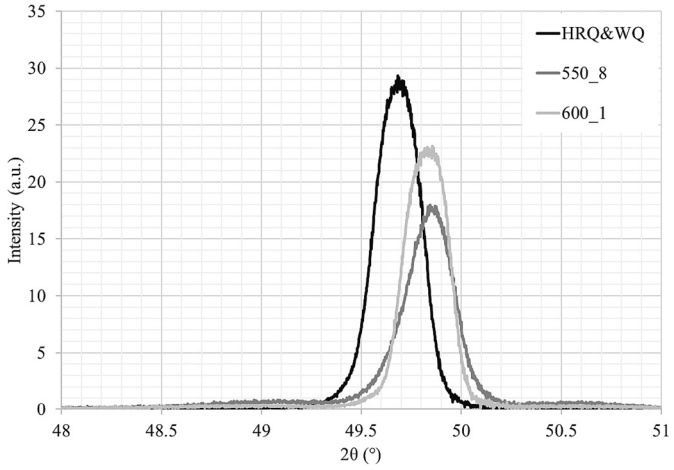

Fig. 8. XRD analysis of the HR&WQ, 550_8, and 600_1 sample at a 2θ range between 48 and 51°.

the smaller size and fraction of κ-carbides in the 600_1 sample means that the dislocations may move more freely in the austenite matrix by gliding, and the possibility of meeting and shearing a κ-carbide is reduced. This results in the higher elongation that was observed in this

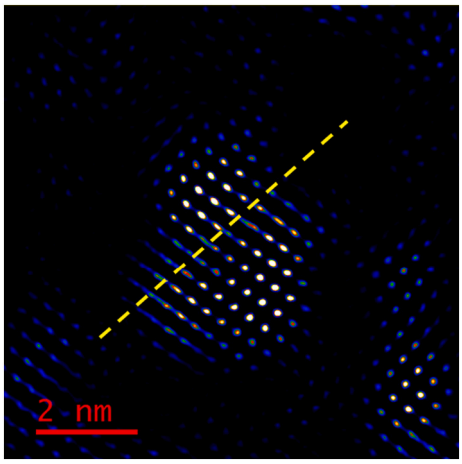

Fig. 9. IFFT image of a κ-carbide in the 550_8 sample after tensile deformation. The destruction of the SRO and the step on the left and right of the yellow line indicate the shearing of the carbide. (For interpretation of the references to colour in this figure legend, the reader is referred to the web version of this article.)

sample. Specifically, a difference of ~1.5 nm in the size of the κ-carbides leads to an increase in the total elongation of approximately 20%. From the Dark Field (DF) TEM image and the selected area diffraction pattern (insert on the top left corner), it is shown that this grain has a zone axis [001] and hence, the κ-carbides can be observed. The micro-bands can also be observed in the Kernel Average Misorientation (KAM) map from the formation of dislocation walls and by the IPF map from the slight difference in colour. As indicated in the literature [19], in order to accumulate the strains, these micro-bands start to rotate. This rotation is also visible in the DF image, as the κ-carbides outside this micro-band cannot be observed. The thickness of the micro-band was also measured from the distance A-B between the dislocation walls from the KAM map, at 260 nm, which corresponds to the observations from the STEM and TEM images. According to the same literature, increasing the strain, will result in decreasing the thickness of the micro-bands.

The level of micro-banding was also studied with EBSD. Different maps were taken on the transverse plane of the tensile sample at different distances from the fracture, as can be seen in Fig. 11. The level of strain depends on the distance to the fractured surface.

From the IPF maps, it can be seen that the austenite grains become more elongated and the level of misorientations increase as the distance from the fracture decreases and the strain increases. This means that the density of microbands is increasing, and they rotate in order to accumulate the additional strain. This is according to the literature [19]. The Kernel Average Misorientation (KAM) maps indicate the level of strain inside the austenite grains, by the fraction of misorientations between the different points of the map. As expected, at higher levels of strain, the level of misorientation increases, with angles between 2 and 3° showing up more frequently (Fig. 11i) under the fracture surface.

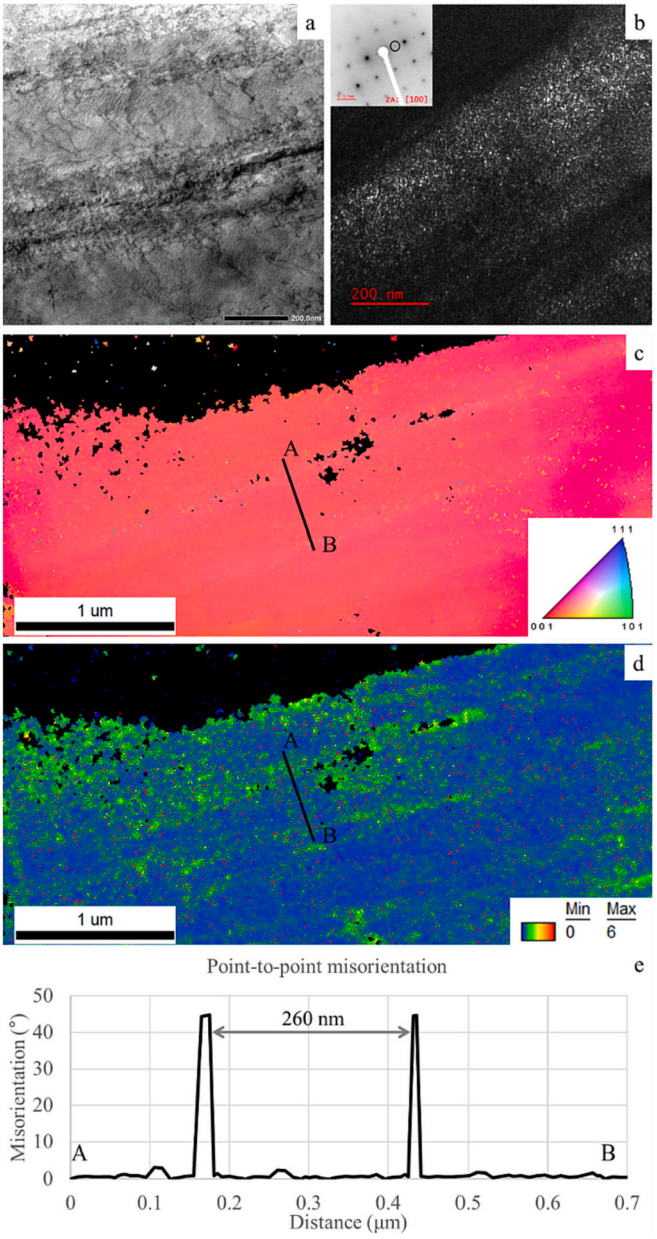

Fig. 10. a) STEM images of the 550_8 sample after tensile testing, showing the micro-bands and the mobile dislocations inside b) DF TEM image of the same area showing the fraction and size of κ-carbides inside the exact microband, c) IPF map of the same area, showing the change in orientation between the micro-bands, d) KAM map of the same grain in TKD, showing the formation of dislocation walls and micro-bands e) point-to-point misorientation, measured from the KAM maps between points A and B.

5. Conclusions

This study has focused on the relationship between the κ-carbide size and the mechanical properties of a Fe-29Mn-8.7Al-0.9C alloy. It has been found that the finer diameter of the precipitates leads to larger channels in the deformed austenitic matrix. These channels act as pathways for the gliding dislocations until they are impinged by the κ-carbides. Then, due to their coherency with the austenite matrix, the carbides are sheared by the dislocations, which glide through the micro-bands, and lead to a reduction of the total elongation of the steel. The impingement of the dislocations leads to the formation of microbands, the density and rotation of which depends on the level of strain. It can be concluded that the greater the number of interactions between the κ-carbides and the gliding dislocations, the more pronounced the reduction of the elongation will be. In this case study, the sample aged at a slightly increased temperature but for much less time, produced ~1.5 nm finer precipitates and hence exhibited much higher elongation (~20%) without significant loss of tensile strength. Hence, this sensitivity needs to be controlled, as such a small difference in the particle size can significantly alter the material properties.

CRediT authorship contribution statement

Alexandros Banis: Conceptualization, Methodology, Validation, Formal analysis, Investigation, Writing – original draft, Visualization.

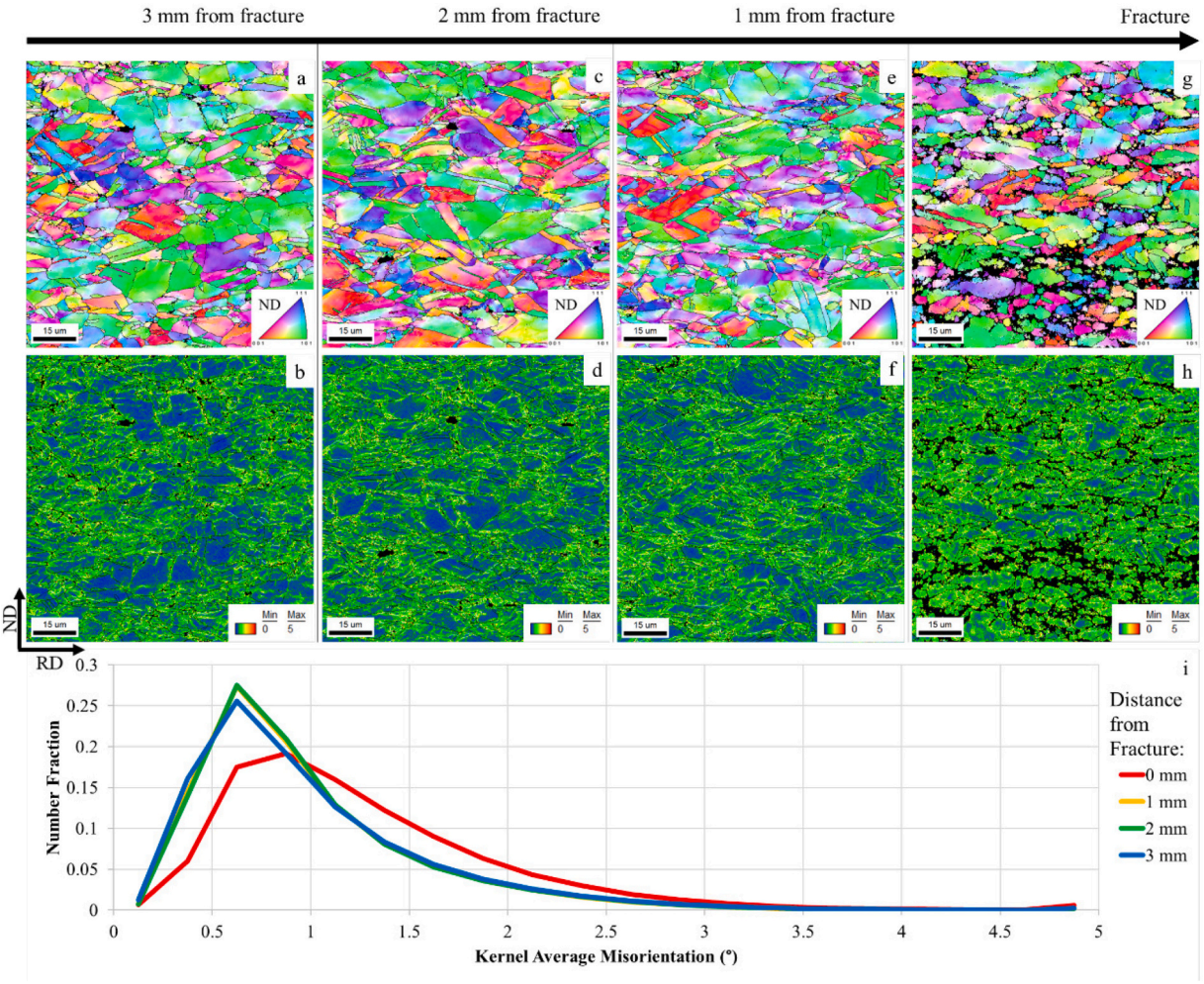

Fig. 11. EBSD IPF and KAM maps of the 550_8 tensile sample, taken from different distances from the fracture. As the distance from the fracture decreases, the level of misorientations inside the austenite increases, corresponding to the higher fraction of microbands.

Andrea Gomez: Formal analysis, Investigation. **Aniruddha Dutta:** Resources. **Ilchat Sabirov:** Supervision, Project administration, Writing – review & editing. **Roumen H. Petrov:** Supervision, Project administration, Resources, Writing – review & editing.

Declaration of Competing Interest

The authors declare that they have no known competing financial interests or personal relationships that could have appeared to influence the work reported in this paper.

Data availability

The raw/processed data required to reproduce these findings cannot be shared at this time due to technical or time limitations.

Acknowledgments

The authors acknowledge the European Union's Research Fund for Coal and Steel via the DELIGHTED project (Grant No. 899332).

References

[1] S. Chen, R. Rana, A. Haldar, R.K. Ray, Current state of Fe-Mn-Al-C low density steels, Prog. Mater. Sci. 89 (2017) 345–391.
[2] O.A. Zambrano, A general perspective of Fe–Mn–Al–C steels, J. Mater. Sci. 53 (2018) 14003–14062.
[3] G. Frommeyer, E. Drewes, B. Engl, Physical and Mechanical Properties of iron-Aluminium-(Mn, Si) Lightweight Steels, Rev. Met. Paris. 97, 2000, pp. 1245–1253.
[4] G. Frommeyer, U. Brüx, Microstructures and mechanical properties of high-strength Fe-Mn-Al-C light-weight TRIPLEX steels, Steel Res. Int. 77 (2006) 627–633.
[5] C.-Y. Chao, C.-H. Liu, Effects of Mn Contents on the microstructure and mechanical properties of the Fe-10Al-xMn-1.0C alloy, Mater. Trans. 43 (2002) 2635–2642.
[6] G.L. Kayak, Fe-Mn-Al precipitation-hardening austenitic alloys, Met. Sci. Heat Treat. 11 (1969) 95–97.
[7] R.A. Howell, T. Weerasooriya, D.C. Van Acken, Tensile, high strain rate compression and microstructural evaluation of lightweight age hardenable cast Fe-30Mn-9Al-XSi-0.9 C-0.5 Mo steel, Trans. Ame. Foundrymen's Soc. 117 (2009) 7–18.
[8] K. Lee, S.-J. Park, J. Moon, J.-Y. Kang, T.-H. Lee, H.N. Han, β-Mn formation and aging effect on the fracture behavior of high-Mn low-density steels, Scr. Mater. 124 (2016) 193–197.
[9] K. Sato, K. Tagawa, Y. Inoue, Spinodal decomposition and mechanical properties of an austenitic Fe-30wt.%Mn-9wt.%Al-0.9wt.%C alloy, Mater. Sci. Eng. A 111 (1989) 45–50.
[10] K. Sato, K. Tagawa, Y. Inoue, Modulated structure and magnetic properties of age-hardenable Fe-Mn-Al-C alloys, MTA 21 (1990) 5–11.
[11] R.A. Howell, D.C. Van Aken, A Literature Review of Age Hardening Fe-Mn-Al-C Alloys, Iron and Steel Technology 6, 2009.
[12] C.Y. Chao, C.N. Hwang, T.F. Liu, Grain boundary precipitation behaviors in an Fe-9.8Al-28.6Mn-0.8Si-1.0C alloy, Scr. Mater. 34 (1996) 75–81.
[13] C.Y. Chao, C.N. Hwang, T.F. Liu, Grain boundary precipitation in an Fe-7.8Al-31.7Mn-0.54C alloy, Scr. Metall. Mater. 28 (1993) 109–114.
[14] Y.H. Tuan, C.L. Lin, C.G. Chao, T.F. Liu, Grain boundary precipitation in Fe-30Mn-9Al-5Cr-0.7C alloy, Mater. Trans. 49 (2008) 1589–1593.
[15] Y. Feng, R. Song, Z. Pei, R. Song, G. Dou, Effect of aging isothermal time on the microstructure and room-temperature impact toughness of Fe–24.8Mn–7.3Al–1.2C austenitic steel with κ-carbides precipitation, Met. Mater. Int. 24 (2018) 1012–1023.

[16] A. Banis, A. Gomez, V. Bliznuk, A. Dutta, I. Sabirov, R.H. Petrov, Microstructure evolution and mechanical behavior of Fe–Mn–Al–C low-density steel upon aging, Mater. Sci. Eng. A 875 (2023) 145109.
[17] M.N. Elkot, B. Sun, X. Zhou, D. Ponge, D. Raabe, Hydrogen-assisted decohesion associated with nano-sized grain boundary κ-carbides in a high-Mn lightweight steel, Acta Mater. 241 (2022) 118392.
[18] S. Allain, J.-P. Chateau, O. Bouaziz, S. Migot, N. Guelton, Correlations between the calculated stacking fault energy and the plasticity mechanisms in Fe–Mn–C alloys, Mater. Sci. Eng. A 387-389 (2004) 158–162.
[19] J.D. Yoo, K.-T. Park, Microband-induced plasticity in a high Mn–Al–C light steel, Mater. Sci. Eng. A 496 (2008) 417–424.
[20] D.P. Field, L.T. Bradford, M.M. Nowell, T.M. Lillo, The role of annealing twins during recrystallization of Cu, Acta Mater. 55 (2007) 4233–4241.
[21] K. Sato, Y. Igarashi, Y. Inoue, T. Yamazaki, M. Yamanaki, Microstructure and age hardening in spinodally decomposed austenitic Fe-Mn-Al-C alloys, in: Stainless Steels: International Conference of Stainless Steels, The Iron and Steel Institute of Japan, Chiba, Japan, 1991.
[22] L.N. Bartlett, D.C. Van Aken, J. Medvedeva, D. Isheim, N. Medvedeva, K. Song, An atom probe study of κ-carbide precipitation in austenitic lightweight steel and the effect of phosphorus, Metall. Mat. Trans. A 48 (2017) 5500–5515.
[23] M.J. Yao, E. Welsch, D. Ponge, S.M.H. Haghighat, S. Sandlöbes, P. Choi, M. Herbig, et al., Strengthening and strain hardening mechanisms in a precipitation-hardened high-Mn lightweight steel, Acta Mater. 140 (2017) 258–273.
[24] I. Gutierrez-Urrutia, D. Raabe, High strength and ductile low density austenitic FeMnAlC steels, Mater. Sci. Technol. 30 (2014) 1099–1104.
[25] S.-D. Kim, S.-J. Park, J.H. Jang, J. Moon, H.-Y. Ha, C.-H. Lee, H. Park, et al., Strain hardening recovery mediated by coherent precipitates in lightweight steel, Sci. Rep. 11 (2021) 14468.
[26] B. Mishra, A. Mukhopadhyay, R. Sarkar, M.K. Kumawat, V. Madhu, M.J.N. V. Prasad, Strain hardening and stored energy in high-Mn austenitic based low-density steel, Mater. Sci. Eng. A 861 (2022) 144331.
[27] S. Li, D. Li, H. Lu, P. Cao, R. Xie, Effect of κ carbides on deformation behavior of Fe-27Mn-10Al-1C low density steel, Crystals 12 (2022) 991.
[28] H. Kim, D.-W. Suh, N.J. Kim, Fe-Al-Mn-C lightweight structural alloys, Sci. Technol. Adv. Mater. 14 (2013) 14205.
[29] I. Gutierrez-Urrutia, D. Raabe, Influence of Al content and precipitation state on the mechanical behavior of austenitic high-Mn low-density steels, Scr. Mater. 68 (2013) 343–347.